Interplay between local structure and magnetic properties of graded exchange-coupled Co@FePt nanocomposite films

Charles Paleo, Véronique Dupuis, Fabrice Wilhelm, Andrei Rogalev, Olivier Proux, Olivier Boisron, Isabelle Kieffer, Thierry Epicier, Matthieu Bugnet, Damien Le Roy

Interplay between local structure and magnetic properties of graded exchange-coupled Co@FePt nanocomposite films

Charles Paleo,[1,*] Véronique Dupuis,[1] Fabrice Wilhelm,[2] Andrei Rogalev,[2] Olivier Proux,[3] Olivier Boisron,[1] Isabelle Kieffer,[3] Thierry Epicier,[4] Matthieu Bugnet,[4] and Damien Le Roy[1]

[1] *Institut Lumière Matière, Université Claude Bernard Lyon 1, CNRS, F-69622, Villeurbanne, Cedex, France*
[2] *The European Synchrotron Radiation Facility (ESRF), 38000 Grenoble, France*
[3] *Observatoire des Sciences de l'Univers de Grenoble, UMS 832, CNRS—Université Grenoble Alpes, 38041 Grenoble cedex 9, France*
[4] *INSA-Lyon, Université Claude Bernard Lyon 1, CNRS, 7 Avenue Jean Capelle, F-69621 Villeurbanne, Cedex, France*

(Dated: September 15, 2020)

Magnetically-hard nanocomposites are attractive materials for integration in various microsystems and for building next generation permanent magnets. However, exploiting their full potential requires to control their microstructure at the nanometre scale. Studying these materials in model systems synthesised by nanofabrication routes gives interesting insights about the interplay between the microstructure and the magnetic performances. Here, by using a combination of mass-selected low energy cluster beam deposition and electron-beam evaporation, we have prepared nanocomposite films where Co nanoinclusions are integrated in a hard magnetic FePt matrix. Local atomic structures and element selective magnetic properties of such nanocomposites have been thoroughly investigated using polarisation dependent hard X-ray absorption spectroscopies. These results demonstrate that magnetically soft inclusions are stabilised at room temperature, emphasising the role of the interdiffusion in the preparation of nanocomposites.

I. INTRODUCTION AND BACKGROUND

Hard magnetic materials with high magnetisation are attracting a lot of attention for various applications, from spintronics [1] to magnetic recording media [2, 3] or in bulk permanent magnet for energy conversion technologies [4]. The figure of merit of a permanent magnet is the so-called energy product $(\mathrm{BH})_{max} \leq \frac{1}{4}\mu_0 M_s^2$. The limit is attained for an ideal microstructure and an uniaxial texture, which is nearly achieved in NdFeB sintered and oriented magnets. With an outstanding combination of a relatively large magnetisation $\mu_0 M_s$ of 1.61 T and a large magnetocrystalline anisotropy leading term K_1 of 4.3 MJ.m^{-3}, they lead the performances of permanent magnets for about 30 years, approaching the $(\mathrm{BH})_{max}$ theoretical limit of 516 kJ.m^{-3} for these non-nanostrucuted elements [4]. Designing a hard magnetic material with magnetisation $\mu_0 M_s$ higher than 1.61 T is a necessary -although not sufficient- condition to surpass the performances of nowadays best rare earth (RE) magnets. Fe-Co alloys could be among the most attractive candidates for permanent magnets, with $\mu_0 M_s \geq 1.81$ T for pure Co and up to $\mu_0 M_s = 2.45$ T for $Fe_{65}Co_{35}$. In the latter case, it could push the limit of reachable $(\mathrm{BH})_{max}$ up to nearly 1.2 MJ.m^{-3}, if a square magnetisation loop with a coercive field in excess of 1.2 T could be achieved ($\mu_0 H_c \geq \frac{\mu_0 M_s}{2}$). However, this relies on our ability to significantly increase the relatively low magnetocrystalline anisotropy ($K_1 \leq 20$ kJ.m^{-3})[5], so far predicted but not fully achieved experimentally [6].

In addition to these challenges, the risks associated with the sourcing and the fluctuating cost of RE metals due to geostrategic availability, and the pollution during extraction of the raw elements and recycling of the used materials are driving the need to reduce the dependency to the REs in high performance permanent magnets[7–9]. An elegant approach to design a magnet with high value of energy product was proposed by Kneller and Harwig, that consists in fabrication of a nano-composite (NC) materials combining a hard magnetic phase exchange coupled to a strongly magnetic soft phase [10]. The beneficial effect of this approach was initially demonstrated in 1989 by Coehoorn on $Nd_2Fe_{14}B$-Fe_3B ribbons [11]. This finding stimulated further investigations, including theoretical and modelling studies to optimise the NC structure [10, 12]. In order to develop new magnets with unprecedented performances, the volume fraction of the hard magnetic phase should be limited to the minimum needed to fulfil the coercive field criterion [13]. Under the assumptions of zero magnetic anisotropy in the softer phase and sharp interface between soft and hard magnetic phases, the maximum size of the soft phase regions is twice the size of the domain wall width of the hard phase. Therefore, to exploit the full potential of nanocomposite magnets, one needs to control their microstructure at the nanometre scale, including the size of the soft inclusions, their concentration and the roughness of the interface between the hard and soft phases. In this context, nanocomposite films made from nanofabrication routes are foreseen to bring interesting insights in view of guiding the synthesis of bulk systems[14, 15].

In this work, we investigate the principle of thin-film nanocomposite magnets of Co nanometre-sized grains embedded in a hard FePt matrix (named Co@FePt). The

* charles.paleo@univ-lyon1.fr

fine microstructure analysis requires techniques allowing the chemical distinction of Fe and Co at the nanometric scale. The chemically ordered $L1_0$-FePt phase presents a magnetocrystalline anisotropy K_1 of 6.6 MJ.m^{-3} and a magnetisation of $\mu_0 M_s = 1.43$ T (a maximum $(BH)_{max}$ of 407 kJ.m^{-3}), slightly inferior to the one of NdFeB [5]. Besides, the use of expensive elements like Pt for bulk magnets is excluded. However, when it comes to microtechnologies where the fabrication costs generally dominate over the raw material costs, FePt films can be of great interest. Indeed, they offer higher resistance against corrosion, as compared to RE-based films, which makes them more compatible with standard microfabrication processes. NC films of Co_{50}@$(FePt)_{50}$ would potentially exhibit 28% higher $(BH)_{max}$ than the $L1_0$-FePt alone.

To prepare the nanocomposites samples, a first layer of Co clusters is deposited on a Si substrate, then a 1.15 nm film of Fe, then a 1.40 nm third film of Pt from electron-gun evaporation. These three steps are repeated six times in total.

CoFePt nanofilms (NF) samples are prepared entirely by electron gun evaporation, with the same atomic Co content as NC samples. Finally, a $L1_0$-FePt NF without Co was prepared as a reference ($L1_0$-FePt ref.).

The transition of FePt layers to the magnetically hard $L1_0$-FePt phase was obtained by thermal annealing [16] (see Methods for details and Supporting Information Fig. S1).

The mean size of mass-selected Co clusters is around 7.9 nm in diameter, as obtained from transmission electron microscopy (TEM) observation (Fig. 1a and b). To verify the cluster diameter in the FePt matrix, a single Co cluster layer embedded between two FePt on a Si_3N_4 substrate has been prepared to perform energy-dispersive X-ray (EDX) images, provided in Fig. 1c, where the clusters observed in the metallic matrix have a size compatible with the diameter found by TEM imaging.

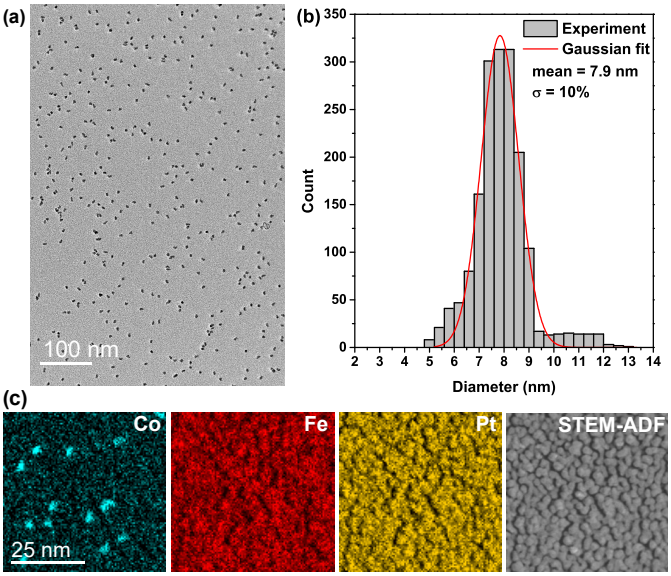

FIG. 1. **(a)** Bright field TEM image of the mass-selected Co clusters protected by a C film. **(b)** Size histogram deduced from TEM observations along with the Gaussian fit. **(c)** EDX images of a FePt/Co clusters/FePt sample on a Si_3N_4 substrate, along with the annular dark-field scanning transmission electron microscopy (STEM-ADF) image. Both measurements give consistent cluster diameter pre-annealing, even when embedded in metallic matrix. The distribution of Fe and Pt is not perfectly homogeneous but reveals "clouds-like" formations, similar to thin films deposition, which most likely disappear when the thickness increases[17].

A. Magnetic properties

The magnetic properties of Co@FePt nanocomposites were studied by superconducting quantum interference device (SQUID) magnetometry and X-ray magnetic circular dichroism (XMCD) experiments performed at room temperature (see SI methods for details [18]).
Fig. 2 presents the magnetisation curves of NC and NF containing 20% Co, and a reference $L1_0$-FePt film ($L1_0$-FePt ref). On the one hand, both NC and NF samples have higher saturation magnetisation than the $L1_0$-FePt ref., which is attributed to the higher magnetisation of Co as compared to FePt. On the other hand, the NC sample exhibits a higher coercivity than the NF, which is magnetically soft as expected for cubic $L1_2$ phase. The remanence magnetisation, measured in plane, is relatively high in all cases (superior to 80%), and indicates no significant out-of-plane c-texture.

Despite the higher magnetisation value of the NC, the estimated energy product $(BH)_{max}$ is lower compared to the one in $L1_0$-FePt ref. because of lower coercive field (Table I).

In the ideal case of a sharp interface between the hard FePt and the soft Co phases, element specific studies permit to separately probe both components. The dependence of the XMCD signal as a function of the applied magnetic field (Fig. 3) shows that Fe and Co exhibit the same behaviour and switch at the same field value for every concentration (in the studied range $0-30$% Co), indicating a strong coupling. Isolated face-centred cubic (fcc) Co clusters with a diameter of 7.9 nm are expected to be superparamagnetic at room temperature and, therefore,

TABLE I. Coercive field and energy product for a NC, a NF, the $L1_0$-FePt ref., and a $Nd_2Fe_{14}B$ random bonded magnet from Coey [19].

	$\mu_0 H_c$ (T)	$(BH)_{max}$ (kJ.m^{-3})
30% Co NC	0.18	63
30% Co NF	0.01	< 1
$L1_0$-FePt ref.	1.4	119
$Nd_2Fe_{14}B$ (random bonded)	~ 0.8	63

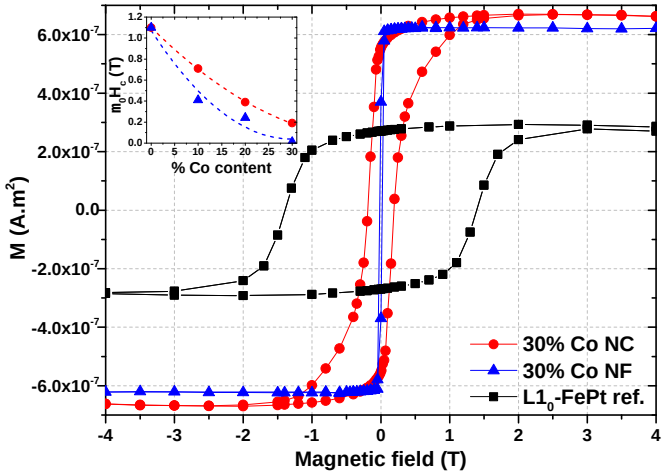

FIG. 2. Hysteresis loops at 300 K for two samples with the same Co content and the FePt matrix without Co. The NC sample has higher saturation magnetisation than the bare $L1_0$-FePt ref. which is brought by the Co, but keeps a sizeable coercivity whereas the NF are magnetically soft. The inset shows the dependence of the coercive field $\mu_0 H_c$ with the Co content for NF and NC (the dashed lines are a guide for the eye).

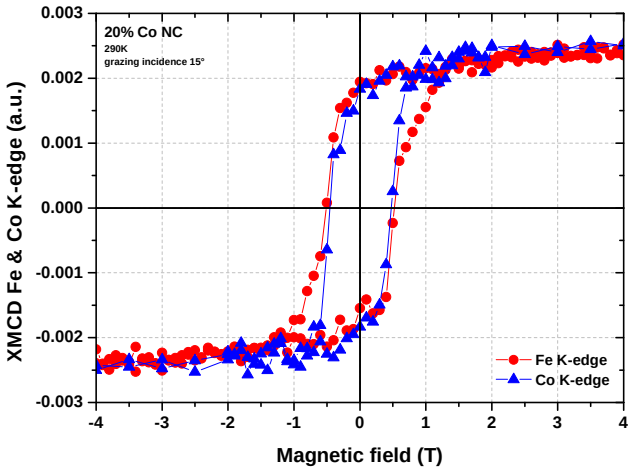

FIG. 3. Hysteresis loops at 290 K of a 20% Co NC sample at Fe and Co K-edges. Both elements show the same coercivity.

magnetically soft. Here, there is no kink at low field on the magnetisation curve, showing that the whole film behaves like a single magnetic phase and there is no indication of the presence of a secondary magnetic phase. However, it does not give access to the degree of interdiffusion at the cluster-matrix interface, which may lead to different intermixing states (as illustrated in Fig. S2). Such an interdiffusion is expected to result in a modulation of the composition with an intermediate diffused layer between a Co core and a FePt matrix that could be denoted as (Co@$Co_xFe_yPt_z$@FePt). The ultimate stage of interdiffusion would be a homogeneous alloyed film, which is rather unlikely as the magnetic properties of NC differ significantly from the reference homogeneous NF.

Apart from the latter hypothesis of a homogeneous configuration, definitely ruled out by SQUID magnetometry measurements, it would be very difficult to discern between non cluster-matrix interdiffusion and Co@$Co_xFe_yPt_z$@FePt by TEM imaging. X-ray absorption spectroscopy (XAS) studies have thus been performed to clarify the local structural properties of the samples.

B. Structural properties

X-ray absorption near edge structure (XANES) and XMCD signals at the Co K-edge are presented in Fig. 4, for a 20% Co NC sample and references Co hexagonal close-packed (hcp) and $L1_0$-CoPt. The 20% Co NC XANES signal is very different from a Co fcc signal, which shows an important dip on A and a B_2 peak at higher energy [20], whereas the NC sample and references have a symmetric B_1 and B_2 feature close to one another, characteristic of face-centred tetragonal (as in $L1_0$-FePt and $L1_0$-CoPt) alloyed phases[20, 21]. This splitting suggests some alloying of Co with Fe and Pt from the matrix in the NC sample, as expected for the $L1_0$-CoPt reference. Nevertheless, the B_1-B_2 splitting is also present in Co hcp[22, 23], and extended X-ray absorption fine structure (EXAFS) measurements were performed to better understand the structure of the NC sample, and will be detailed later. The XMCD signal of the NC is close to the $L1_0$-CoPt signal, demonstrating that Co is not in pure metallic state, neither hcp nor fcc.

X-ray linear dichroism (XLD) measurements at the Fe K-edge for 20% Co NC, NF and the $L1_0$-FePt reference (Fig. S3) reveal significant XLD signal which proves a -at least partial- texturation of the sample, favoured by the alternative stacking of the layers[16]. The XANES peaks B_1 and B_2 appears asymmetric only for NF sample (B_2 feature higher than B_1), which is consistent with an enrichment in Co for NF samples, as observed in other studies[25] and the XANES of the hcp Co.
The shoulder A, mainly due to Co and Fe $4p$ orbitals[21] is larger for the NF, as expected for a more complete mixing in the NF as compared to in the NC.

To study the local structure of the samples, XAS measurement have been performed to obtain the specific EXAFS signature at the Fe and Co K-edges and Pt L_3-edge (see SI methods for details [26, 27]). Fig. 5 presents the modulus and real part of the Fourier transform (FT) of the EXAFS signal for 30% Co NC and NF, giving an additional qualitative indication of different local environments in both systems. The comparison to the $L1_0$-FePt ref. (Fig. S4), shows that the NC is much closer to this phase at the Fe K-edge. This is an argument in favour of a stronger Co-matrix diffusion in the NF than in the

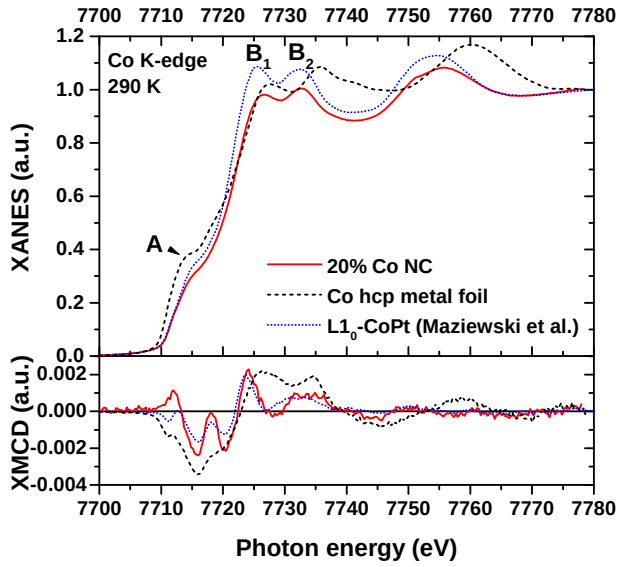

FIG. 4. XANES and XMCD signal at the Co K-edge of a 20% Co NC, a Co hcp metallic foil (from private communication with A. Rogalev and F. Wilhelm) and a $L1_0$-CoPt reference (from Maziewski et al. [24]).

NC, which could also explain the low coercivity obtained on this NF sample. As Co and Fe show similar binary phase diagram with Pt[28], the more atomic interdiffusion occurs, the more the stable phase shifts towards the higher Co+Fe content values, leading to a magnetically soft $L1_2$-X_3Pt (with $X = Co, Fe$).

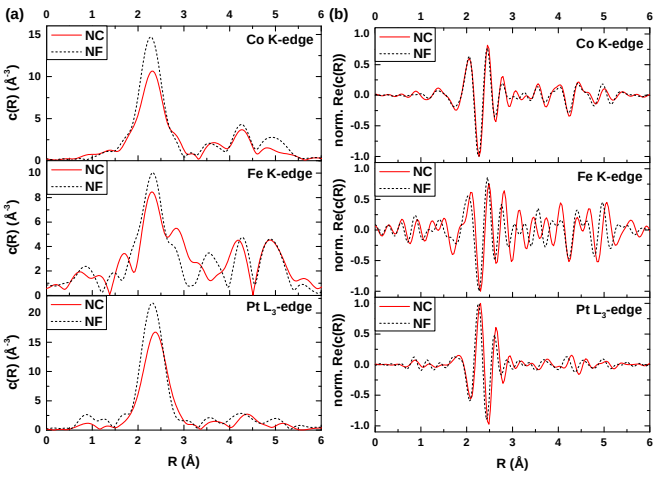

FIG. 5. Comparison of the magnitude **(a)** and real part of the FT **(b)** of the EXAFS signal for 30% Co NC and 30% Co NF at each edge.

Two different kinds of simulation have been realised to analyse the spectra: a first fit is performed on a wide radial distance (typically between 1.5 and 5.5 Å) at each edge, with different possible crystal alloy phases, by setting the nature and number of neighbouring atoms N_j. The best fits from this method for each edge is provided on Table II (detailed EXAFS results are provided in the SI Tables).

For the 30% NC sample, the EXAFS simulations at the Fe K-edge and Pt L_3-edge lead to $L1_0$-FePt structure. On the contrary, for the NF sample, the optimised structure is a mixed X_3Pt structure at the Fe K-edge and Pt L_3-edge, confirming the strong Co-matrix intermixing in this sample. Distinguishing Fe from Co neighbouring atoms based on EXAFS measurements is a difficult task (as $\Delta Z = 1$). Nevertheless, the fact that the Co_3Pt phase fits only at Co K-edge in the NC samples (Fig. 6) while $L1_0$-FePt phase fits at Fe K and Pt L_3-edge suggests the persistence of Co-rich regions.

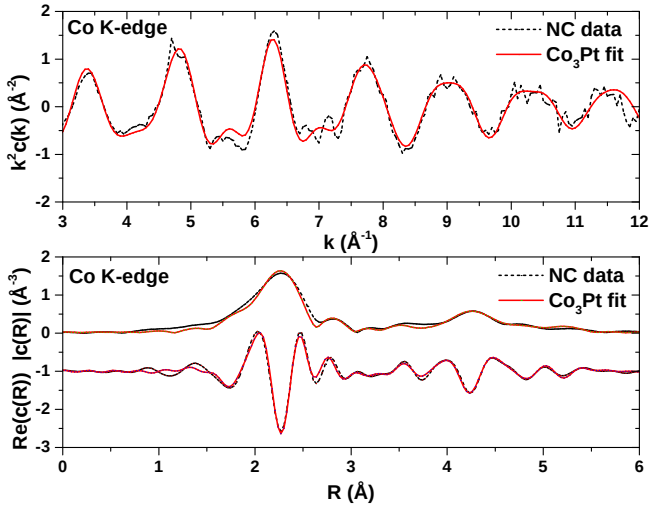

FIG. 6. Weighted EXAFS oscillations, magnitude of the filtered signal, and real part of the FT of the 30% Co NC sample at the Co K-edge, along with the Co_3Pt fit.

To quantify atomic interdiffusion between cluster and matrix in the NC, another fit is performed at the Co K-edge on NC samples, by choosing small radial distances (between 1.5 and 3.0 Å) to limit to the first neighbours of the Co atoms. The fit is realised with Co (accounting for both Co or Fe atoms) and Pt atoms, initially at positions found from the previous Co_3Pt fit. The coordination numbers N_j are then set free (but restraining to $N_{Co,Fe} + N_{Pt} = 12$) and have been obtained by the fit at different angles. The number of Co-Co bonds is found to be in average centred on $N_{Co-Co} = 4.2$ (Fig. S5).

In addition, a diffusion of the cluster is simulated from an initial truncated-octahedron Co cluster (stable shape

TABLE II. Structure giving the best fits for a window between 1.5 and 5.5 Å ($X = Co, Fe$).

Best fit at	NC	NF
Co K-edge	X_3Pt	X_3Pt
Fe K-edge	$L1_0$-FePt	X_3Pt
Pt L_3-edge	$L1_0$-FePt	X_3Pt

of fcc clusters[29]) of 11 atoms/ridge (which size corresponds to the size observed by TEM) inserted in a FePt matrix. A simple iterative diffusion algorithm is then applied to every atom by giving a 50% probability of swapping its place with a neighbouring atom. The mean number of Co-Co bonds is then calculated and compared to the number obtained by EXAFS fitting. These steps are repeated until the coordination number of the model is equal or lower than the one obtained from the EXAFS. It results that this 4.2 coordination number can occur when matrix atoms reach the centre of the cluster (Fig. S6), but the Co concentration remains above 75% in a 1.8 nm radius at least.
For NC, the important criterion is the core size of the soft inclusion. According to the Co-Pt (or Fe-Pt) phase diagrams, the edge of the $L1_0$ phase is at least 35% content in Co (or Fe)[28]. Therefore, with Co-content clusters embedded in hard $L1_0$ matrix, the soft inclusion of X_3Pt remains around 7.4 nm diameter after annealing (Fig. S7).

II. CONCLUSION

Magnetic measurements of the composition dependence of the coercive field as well as the EXAFS fitting and simulation treatment prove that, after annealing at 700°C for 20 min, NC still present high Co content inclusions, contrary to the NF where the interdiffusion is complete. To explain such result, one can first mention that clusters have a well-defined shape as prepared and are particularly stable[30]. Secondly, for the same amount of Co in a sample, the thickness of the Co layer in NF (1.0 nm for 30% Co) is smaller than the radius of a cluster as prepared, favouring the total Co-atomic diffusion in matrix during annealing. This lower diffusion in NC allows the matrix to stay in the $L1_0$ stability domain, keeping the magnetic hardness of the sample.
Moreover, the cluster diffusion simulation does not take into account the different miscibility as well as the different sizes of Fe, Co, or Pt atoms, which can lead to different diffusion coefficients[28]. As such, heavy Pt atoms of the matrix are less likely to diffuse into the Co cluster. The crystal distortions of the fcc Co-rich regions in the face-centred tetragonal (fct) $L1_0$ matrix have also been neglected in the simulation, but are revealed by the EXAFS fitting.

One of the key factor to improve the $(BH)_{max}$ is a better control of the cluster-matrix interdiffusion: with thinner layers of Fe and Pt and a larger number of repetition, the annealing to form the $L1_0$ phase can be achieved at lower temperature and faster. Moreover the maximum of coercivity for non-epitaxial thin films is not reached for $Fe_{50}Pt_{50}$, but rather for $Fe_{53}Pt_{47}$[31, 32]. Although pure Co clusters provide the opportunity to visualise soft and hard phases individually, they are not in favour of a high $(BH)_{max}$, as the highest moment per atom is reached for $Fe_{65}Co_{35}$[5]. Finally, the texturation of the hard magnetic matrix could be improved using a MgO crystal substrate. These Co@FePt samples are a proof of concept of NC permanent magnets, stabilising the moments of the soft clusters at room temperature.

III. METHODS

A. Sample Preparation

These Co@FePt transition metal-based nanocomposite are made from Co soft clusters embedded in a $L1_0$-FePt matrix: the clusters are pre-formed in the gas phase using a laser vaporisation source working in a Low Energy Cluster Beam Deposition (LECBD) system[33]. Deposited in a soft landing regime, the clusters are not fragmented or distorted at the impact on the substrate. Moreover, a quadrupolar electrostatic mass-deviator allows to tighten the size dispersion and to obtain a Gaussian distribution centred at a desired mean value ranging from 2 to 10 nm [34].

The ultra-high vacuum chamber (base pressure in the range of 10^{-10} mbar) is equipped with an electron-beam evaporator with three targets (Fe, Pt and Co) that serve to grow films (for matrix, references and NF samples) by successive atomic depositions.

The formation of the magnetically hard $L1_0$ phase is thermally activated upon high vacuum annealing at 700°C for 20 min[16, 32, 35]. The chemical ordering has been observed for annealing temperatures higher than 650°C with the appearance of the (001) line owing to stacking of pure element planes. The (001)/(110) peak intensity ratio is greater than the one expected for an isotropic polycrystalline system; which suggests a texture in the film. However, the co-existence of strong (111) and (001) peaks indicate a relatively large angular dispersion in the preferential orientation. Note that similar observations were reported previously in films prepared from alternative deposition of Fe and Pt thin layers[16] where the authors assigned the preferential *c*-axis texture to the growth process.

B. TEM Analysis

Bright field TEM imaging of the mass-selected Co clusters protected by a carbon film was performed in a Jeol 2100 HT, operated at 200 kV. The TEM-EDX experiments were performed in a FEI Titan ETEM G2 60-300, operated at 300 kV. For this purpose, a FePt/Co clusters/FePt specimen was deposited by LECBD directly on the Si_3N_4 membrane of a DENSsolutions Wildfire MEMS chip, maintained at room temperature in the present study.

C. XMCD, XLD and XANES analyses

Polarisation dependent X-ray absorption, XLD and XMCD experiments have been performed at the ID12 beamline [18] of the European Synchrotron Radiation Facility (ESRF). The X-ray source for these measurements was the first harmonic of APPLE-II type helical undulator (HU-38) in a pure helical mode. The X-ray beam was monochromatised with a fixed-exit double-crystal monochromator equipped with a pair of Si(111) crystals. The X-ray absorption spectra were recorded using the total fluorescence yield detection mode. The X-ray fluorescence signal from the samples were collected in the back-scattering geometry, using Si photodiodes. The XLD signal is obtained as a difference between two absorption spectra measured with X-ray polarisation vector being either parallel or nearly perpendicular (80 degrees) to the sample surface. To minimise any eventual experimental artefacts, we kept the sample orientation constant and polarisation of X-rays using a 0.9 mm thick diamond quarter wave plate. X-ray quarter wave plate allowed us to transform the incoming circular polarised beam into two orthogonal linearly polarised beams at each energy point of the scan. The absorption was recorded from the same part of the sample for both polarisations. The local magnetic properties of the Fe and Co sites were studied using XMCD method at the Fe and Co K-edge. Measurements were performed at 295 K and under an applied magnetic field of 4 T provided by a superconducting solenoid. The angle between the sample surface and the applied field is 10 degrees. The XMCD spectra were obtained as the difference between two consecutive XANES spectra recorded with opposite photon helicities of the incoming photons. Measurements were performed for both directions of applied magnetic field parallel and anti-parallel to the incoming X-ray wave vector in order to ensure the absence of experimental artefacts. The element-selective magnetisation curves were recorded by monitoring the intensity of XMCD signal as a function of an applied magnetic field.

D. EXAFS Fitting

The software suite Demeter[26], which includes Athena (data normalisation) and Artemis (simulation), was used. This software allows the fitting of the EXAFS formula signal, allowing for each atomic shell j around the target atom i the determination of N_j the coordination number of the atom i, S_i^2 the reduction factor from multi-electronic effects, F_j the backscattering amplitude, σ_j^2 the Debye-Waller factor, $k = \sqrt{\frac{2em_e}{\hbar^2}(E - E_0)}$ the photoelectron wave vector, λ the mean free path of the photoelectron, r_j the interatomic distance and ϕ_{ij} the phase shift.

After the extraction of the EXAFS signal $\chi(k)$ from the absorption signal, its FT ($\chi(R)$) has been restricted to fit the neighbouring of the absorbing atom. The fitting is done by modelling the expected spectrum with FEFF6, choosing the main paths of the photoelectron, then fitting with more paths as the fitting window is increased to higher radial distances. The S_i^2 parameter, which accounts for the relaxation of the other electrons of the absorbing atom[27], is kept fixed in the fits to a value obtained using pure reference foils of each element: 0.73 for Fe, 0.70 for Co, and 0.84 for Pt. The fitted parameters are: the energy edge E_0, allowed to slightly vary according to the sample, the radial distances R_{eff}, to account for distortion of the tested crystal structure R along the a and c-axis (while maintaining the cell volume for cubic structures), and the Debye-Waller σ.

The $L1_0$-FePt ref. sample provided a calibration mean to the procedure which led to the best fit with the $L1_0$ structure for this film.

ACKNOWLEDGMENTS

The authors thank Florent Tournus (iLM laboratory) for his help on the cluster modelling, Nicholas Blanchard (iLM laboratory) for TEM imaging, and José Penuelas (STMS/INL) for the XRD measurements. The TEM-EDX experiments were performed at the Consortium Lyon St-Etienne de Microscopie. XMCD, XLD, XANES and EXAFS measurements were made at ESRF, on beamline ID12 and French CRG BM30B FAME for the latter. This work is supported by the ANR through the collaborative project SHAMAN (ANR-16-CE09-0019), and the doctoral school ED PHAST 52. The authors are also grateful to the ILMTECH platform for clusters synthesis at PLYRA and SQUID measurements at the Centre de Magnétométrie de Lyon.

[1] T. N. A. Nguyen, Y. Fang, V. Fallahi, N. Benatmane, S. M. Mohseni, R. K. Dumas, and J. Åkerman, [co/pd]–nife exchange springs with tunable magnetization tilt angle, Applied Physics Letters **98**, 172502 (2011).

[2] D. Mitin, M. Wachs, N. Safonova, O. Klein, and M. Albrecht, Exchange coupled l10 fecupt/fe heterostructures: Magnetic properties and reversal behavior at elevated temperatures, Thin Solid Films **651**, 158–162 (2018).

[3] B. Ma, G. Y. Situ, H. G. Chu, and J. P. Wang, Exchange coupled composite fept/tbco/[co/ni]n films with an tbco interlayer, AIP Advances **7**, 056508 (2017).

[4] J. Coey, Perspective and prospects for rare earth permanent magnets, Engineering **6**, 119–131 (2020).

[5] J. M. D. Coey, *Magnetism and Magnetic Materials*, 1st ed. (Cambridge University Press, 2001).

[6] T. Burkert, L. Nordström, O. Eriksson, and O. Heinonen, Giant magnetic anisotropy in tetragonal feco alloys, Physical Review Letters **93**, 027203 (2004).

[7] J. Lucas, P. Lucas, T. Le Mercier, A. Rollat, and W. Davenport, *Rare earths: science, technology, production and use* (Elsevier, 2015).

[8] P. Mcguiness, O. Akdogan, A. Asali, S. Bance, F. Bittner, J. M. D. Coey, N. M. Dempsey, J. Fidler, D. Givord, O. Gutfleisch, and et al., Replacement and original magnet engineering options (romeos): A european seventh framework project to develop advanced permanent magnets without, or with reduced use of, critical raw materials, JOM **67**, 1306–1317 (2015).

[9] J. Rial, P. Švec, E. Palmero, J. Camarero, P. Švec, and A. Bollero, Severe tuning of permanent magnet properties in gas-atomized mnal powder by controlled nanostructuring and phase transformation, Acta Materialia **157**, 42–52 (2018).

[10] E. Kneller and R. Hawig, The exchange-spring magnet: a new material principle for permanent magnets, IEEE Transactions on Magnetics **27**, 3588–3560 (1991).

[11] R. Coehoorn, D. De Mooij, and C. De Waard, Meltspun permanent magnet materials containing fe3b as the main phase, J. Magnet. Magnet. Mater **80**, 101–104 (1989).

[12] R. Skomski and J. M. D. Coey, Giant energy product in nanostructured two-phase magnets, Physical Review B **48**, 15812–15816 (1993).

[13] X. Li, L. Lou, W. Song, G. Huang, F. Hou, Q. Zhang, H.-T. Zhang, J. Xiao, B. Wen, and X. Zhang, Novel bimorphological anisotropic bulk nanocomposite materials with high energy products, Advanced Materials **29**, 1606430 (2017).

[14] X. Rui, J. Shield, Z. Sun, L. Yue, Y. Xu, D. Sellmyer, Z. Liu, and D. Miller, High-energy product exchange-spring fept/fe cluster nanocomposite permanent magnets, Journal of Magnetism and Magnetic Materials **305**, 76–82 (2006).

[15] M. Yue, X. Zhang, and J. P. Liu, Fabrication of bulk nanostructured permanent magnets with high energy density: challenges and approaches, Nanoscale **9**, 3674–3697 (2017).

[16] H. Zeng, M. L. Yan, N. Powers, and D. J. Sellmyer, Orientation-controlled nonepitaxial l10 copt and fept films, Applied Physics Letters **80**, 2350–2352 (2002).

[17] A. I. Figueroa, J. Bartolomé, L. M. García, F. Bartolomé, O. Bunău, J. Stankiewicz, L. Ruiz, J. M. González-Calbet, F. Petroff, C. Deranlot, and et al., Structural and magnetic properties of granular co-pt multilayers with perpendicular magnetic anisotropy, Physical Review B **90**, 174421 (2014).

[18] A. Rogalev and F. Wilhelm, Magnetic circular dichroism in the hard x-ray range, The Physics of Metals and Metallography **116**, 1285–1336 (2015).

[19] J. Coey, Perspective and prospects for rare earth permanent magnets, Engineering **6**, 119–131 (2020).

[20] J.-I. Park, M. G. Kim, Y.-w. Jun, J. S. Lee, W.-r. Lee, and J. Cheon, Characterization of superparamagnetic core-shell nanoparticles and monitoring their anisotropic phase transition to ferromagnetic solid solution nanoalloys, Journal of the American Chemical Society **126**, 9072–9078 (2004).

[21] N. M. Souza-Neto, A. Y. Ramos, H. C. N. Tolentino, and Y. Joly, Depth dependent local structures in copt thin films, Journal of Physics: Conference Series **190**, 012112 (2009).

[22] Y. A. Kozinkin, A. A. Novakovich, A. V. Kozinkin, R. V. Vedrinskii, Y. V. Zubavichus, and A. A. Veligzhanin, Mechanisms of formation of near-edge fine structure of k x-ray absorption spectra of metallic cu, ni, co (hcp and fcc phases), and cr, Physics of the Solid State **53**, 1–5 (2011).

[23] P. Mazalski, I. Sveklo, Z. Kurant, K. Ollefs, A. Rogalev, F. Wilhelm, J. Fassbender, L. T. Baczewski, A. Wawro, and A. Maziewski, Xas and xmcd studies of magnetic properties modifications of pt/co/au and pt/co/pt trilayers induced by ga+ ions irradiation, Journal of Synchrotron Radiation **22**, 753–759 (2015).

[24] A. Maziewski, P. Mazalski, Z. Kurant, M. O. Liedke, J. McCord, J. Fassbender, J. Ferré, A. Mougin, A. Wawro, L. T. Baczewski, and et al., Tailoring of magnetism in pt/co/pt ultrathin films by ion irradiation, Physical Review B **85**, 054427 (2012).

[25] E. K. Hlil, R. Baudoing-Savois, B. Moraweck, and A. J. Renouprez, X-ray absorption edges in platinum-based alloys. 2. influence of ordering and of the nature of the second metal, The Journal of Physical Chemistry **100**, 3102–3107 (1996).

[26] B. Ravel and M. Newville, Athena, artemis, hephaestus: data analysis for x-ray absorption spectroscopy using ifeffit, Journal of Synchrotron Radiation **12**, 537–541 (2005).

[27] B. K. Teo, *EXAFS: Basic Principles and Data Analysis* (Springer Berlin, 2014).

[28] C. J. Smithells, W. F. Gale, and T. C. Totemeier, *Smithells metals reference book*, 8th ed. (Elsevier Butterworth-Heinemann, 2004).

[29] R. Van Hardeveld and F. Hartog, The statistics of surface atoms and surface sites on metal crystals, Surface Science **15**, 189–230 (1969).

[30] R. Ferrando, *Structure and properties of nanoalloys*, Frontiers of nanoscience (Elsevier, 2016).

[31] M. Watanabe and M. Homma, Perpendicular magnetization of epitaxial fept(001) thin films with high squareness and high coercive force, Japanese Journal of Applied Physics **35**, L1264–L1267 (1996).

[32] M. H. Hong, K. Hono, and M. Watanabe, Microstructure of fept/pt magneticthin films with high perpendicular coercivity, Journal of Applied Physics **84**, 4403–4409 (1998).

[33] V. Dupuis, G. Khadra, A. Hillion, A. Tamion, J. Tuaillon-Combes, L. Bardotti, and F. Tournus, Intrinsic magnetic properties of bimetallic nanoparticles elaborated by cluster beam deposition, Physical Chemistry Chemical Physics **17**, 27996–28004 (2015).

[34] R. Alayan, L. Arnaud, A. Bourgey, M. Broyer, E. Cottancin, J. R. Huntzinger, J. Lermé, J. L. Vialle, M. Pellarin, and G. Guiraud, Application of a static quadrupole deviator to the deposition of size-selected cluster ions from a laser vaporization source, Review of Scientific Instruments **75**, 2461–2470 (2004).

[35] Y. Liu, T. A. George, R. Skomski, and D. J. Sellmyer, Aligned and exchange-coupled l10 (fe,co)pt-based magnetic films, Journal of Applied Physics **111**, 07B537 (2012).